Synthesis of Lamellar Sodium Tungsten Bronze via Self-assembly Molecular Template and Its Thermoelectric Properties

Maneeyom Sasikan
Department of Applied Science for Electronics and Materials, Interdisciplinary Graduate School of Engineering Sciences, Kyushu University

Ohtaki, Michitaka
Department of Applied Science for Electronics and Materials, Interdisciplinary Graduate School of Engineering Sciences, Kyushu University

https://doi.org/10.5109/7342469

出版情報：Evergreen. 12 (1), pp.494-503, 2025-03. Interdisciplinary Graduate School of Engineering Sciences, Kyushu University, Japan
バージョン：

Synthesis of Lamellar Sodium Tungsten Bronze via Self-assembly Molecular Template and Its Thermoelectric Properties

Maneeyom Sasikan[1], Ohtaki Michitaka[1,2,*]

[1]Department of Applied Science for Electronics and Materials,
Interdisciplinary Graduate School of Engineering Sciences, Kyushu University, Japan

[2]Transdisciplinary Research and Education Center for Green Technologies, Kyushu University, Japan

*Author to whom correspondence should be addressed:
E-mail: ohtaki@kyudai.jp

(Received December 16, 2024; Revised February 17, 2025; Accepted February 19, 2025).

Abstract: An alternating layered structure of sodium tungsten bronze and cetyltrimethylammonium bromide bilayer micellar template was successfully prepared via a one-pot synthesis at 80°C for 2 h. The layered structure was confirmed by X-ray diffraction technique and transmission electron microscopy. Intermolecular interaction between the organic bilayer micelles and the inorganic tungsten oxide layer was observed. Furthermore, the sintered sample was prepared via a conventional method after the removal of the organic templating moiety. Subsequently, its thermoelectric properties were measured at temperatures up to 800°C in an Ar atmosphere. An improved Seebeck coefficient was achieved as a result of the unconventional morphology in the bulk sample.

Keywords: layered structure; sodium tungsten bronze; reduction reaction; self-assembly template; thermoelectric properties

1. Introduction

Nonstoichiometric tungsten oxides (WO_x) can form in various crystal structures, each of which possesses distinguish physical and electrical properties from one another and from the stoichiometric tungsten oxides such as WO_3 and WO_2[1-3]. Sodium tungsten bronze (Na_xWO_3) is one of the nonstoichiometric tungsten oxides with Na ions inserted into the tungsten oxide crystal structure with corner-sharing WO_6 octahedra framework. By adjusting the concentration of the Na ions, not only their crystal structures vary from tetragonal to cubic[4,5] but also their electrical transport properties change from semiconductor ($x < 0.3$) to metallic ($x > 0.3$)[6]. The reason is due to the donation of electrons from the Na ions to the conduction band of the tungsten oxide[7,8]. It was also reported that the effective number of conduction electrons of this type of compound increased with the increasing of numbers of sodium atoms per unit volume[9]. So far, this type of compound has been studied mainly for near-infrared (NIR)-shielding[10], electrochromic[11], plasmonic[12], and photocatalytic[13] applications. However, with its high electrical conductivity, low cost, and nontoxicity, Na_xWO_3 can be promising to be studied as thermoelectric materials, in which the electrical conductivity is one of the important parameters. Furthermore, the microstructure and/or nanostructure controls of this material are good strategies to tune their thermal conductivity and the Seebeck coefficient, which are also key factors to achieve high thermoelectric performance.

Na_xWO_3 has been synthesized via solid-state reaction[14], reduction reactions[15-17], hydrothermal synthesis[18-20], and electrolysis growth[21,22], out of which hydrothermal synthesis is the most well-known technique to achieve Na_xWO_3 nanostructures. These methods are usually highly energy-consuming and/or time-consuming. However, among these routes, the simple reduction reaction between Na_2WO_4 and $NaBH_4$ in the form of a solution has been reported to be done in ambient conditions and conveniently yielded the amorphous Na_xWO_3 within only two hours[17]. Moreover, the amount of the Na ions intercalated in the tungsten bronze structure is controllable by varying the pH and the reaction time. Hence, this reduction reaction provides an effective route to prepare Na_xWO_3 compounds with relatively low energy and time consumption, in comparison to other methods. Nevertheless, study on the nanostructure controlling aspect of this facile route is still lacking.

A soft template constructed from micellar structures of the organic surfactant molecules has been utilized to fabricate nanostructures in both top-down and bottom-up approaches, especially for metal oxide materials[23-26], and is normally applied with a hydrothermal process. This

molecular self-assembly template is formed at an optimum concentration of surfactant molecules in water with the presence of metal ions usually bonded to the head group of the surfactant molecules. Then, metal oxide nanostructures are synthesized under specific conditions and concentration ratios. One of the distinct metal oxide nanostructures synthesized by this technique was lamellar titanium oxide prepared by surfactant bilayer templating[25]. In this case, sodium dodecyl phosphate (SDP) was used as a surfactant during the hydrothermal treatment at 120 °C. By changing the inorganic layers in this structure into highly electrically conductive metal oxides, this lamellar structure could yield unconventional electrical and/or thermal transport properties that have never been reported before. It is also worth noting that such a self-assembly structure of surfactant molecules can be formed under various conditions even in air at room temperature, depending on the types of surfactants. Hence, it is possible to employ the self-assembly template by selecting a suitable surfactant at the optimum concentration ratio and include it into the reduction reaction of Na_2WO_4 to fabricate the Na_xWO_3 nanostructure with a long-range order.

In this study, we report a successfully fabricated lamellar cetyltrimethylammonium bromide (CTAB)-Na_xWO_3 via a simple reduction reaction assisted by a self-assembly template. Its layered structure was studied and observed by X-ray diffraction technique and transmission electron microscopy (TEM). The composition of the compound was confirmed by X-ray photoelectron spectroscopy (XPS) and energy-dispersive X-ray spectroscopy (EDS) on the field-emission scanning electron microscope (FE-SEM). In addition, the interaction between inorganic and organic layers was detected by Fourier-transform infrared spectroscopy (FT-IR). Moreover, we also report its bulk thermoelectric properties after removing the organic templating structure and sintering.

2. Experimental procedure

2.1 Preparation of lamellar Na_xWO_3

Commercially available $Na_2WO_4.2H_2O$ (Fujifilm Wako Pure Chemical Corporation, 99.0-100.5%), $NaBH_4$ (Fujifilm Wako Pure Chemical Corporation), sodium dodecyl phosphate (SDP) (Kyoto Chemical Industry co., Ltd., >75.0%), and cetyltrimethylammonium bromide (CTAB) (Wako Pure Chemical Industries, Ltd.) were used as starting materials.

Na_xWO_3 was prepared via reduction reaction with and without the presence of surfactant molecules. The concentration ratio between Na_2WO_4 and $NaBH_4$ was the same in both cases. The reduction reaction is written as follows.

$$Na_2WO_4 + NaBH_4 + (3\text{-}x)\ H_2O \rightarrow Na_xWO_3 + NaBO_2 + (2\text{-}x)\ NaOH + (4\text{-}0.5x)\ H_2$$

The lamellar structure of Na_xWO_3 was prepared with the concentration ratio of the surfactant molecules (SDP or CTAB) to the metal ions of 0.3:1. 0.01 mol of $Na_2WO_4.2H_2O$ and 0.003 mol of CTAB were dissolved in 40 mL of deionized water (DI water) at 80 °C under moderate stirring. After a homogeneous solution was obtained, 1.80 mL of 1M HCl was added, and the mixture was stirred continuously for 15 min. Consequently, 0.0250 mol (excess amount) of solid $NaBH_4$ was added gradually into the solution, and it was kept stirred for 2 h. The precipitates were separated by centrifugation technique and washed with DI water until the pH became neutral. Then, the precipitates were dried in a vacuum oven at 50 °C for 10 h.

2.2 Characterization

To study the layered structure, powder X-ray diffraction (PXRD) data was collected by using a Rigaku MiniFlex 600 diffractometer (Cu Kα radiation at 40 kV and 15 mA) and the 2θ range was from 2° to 90° with a scanning step $\Delta 2\theta = 0.01°$. The samples were also observed by Titan Cubed G2 (Thermo Fisher Scientific Inc.) operated under the scanning transmission electron microscopy (STEM) mode. Subsequently, the interplanar distance was calculated by using ImageJ software and was compared to the value obtained from the XRD data.

The microstructure and composition of the sample were perceived by a JEOL JSM-IT700HR field-emission scanning electron microscope (FE-SEM) apparatus equipped with energy-dispersive X-ray spectroscopy (EDS). The oxidation states of tungsten were evaluated by X-ray photoelectron spectroscopy (XPS) on a Kratos AXIS-ULTRA with an Al Kα radiation source. The XPS measurement was performed at room temperature and the binding energies of the spectra were calibrated with the C 1s peak of graphite at 284.6 eV. Moreover, information on the interaction between the organic and inorganic layers was also obtained through Fourier-transform infrared spectroscopy (FT-IR). The FT-IR measurement was carried out in a transmittance mode on a JASCO FT/IR-4200 apparatus in the wavelength range from 400 to 4000 cm^{-1} at room temperature. Optical properties were also analyzed on a JASCO V-570 spectrophotometer at the wavelength range from 220 to 900 nm.

2.3 Thermoelectric properties

The lamellar Na_xWO_3 sample was pressed into a 10 mm diameter pellet under a uniaxial pressure of 50 MPa followed by a cold isostatic press (CIP) under 100 MPa for 1 h and heated in air at 350℃ for 2 h to remove the organic moieties. Subsequently, the sample was reground and pressed into a pellet under the same conditions as the previous step. The pellet was then sintered in a tube furnace at 800℃ for 2 h in an N_2 atmosphere.

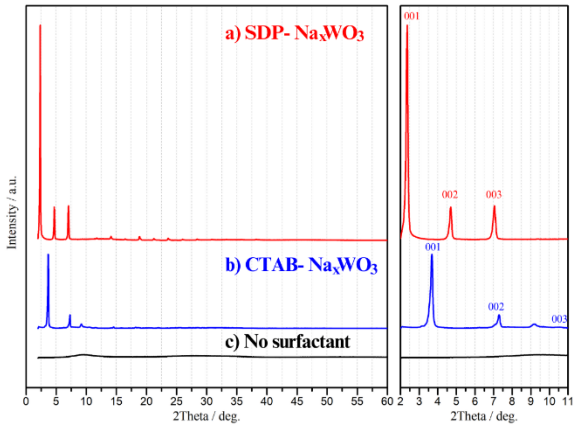

Fig. 1: XRD patterns of Na_xWO_3 synthesized by a reduction reaction (a) with SDP as a surfactant, (b) with CTAB as a surfactant, and (c) without surfactant.

Table 1. The *d* spacings of the samples synthesized with different surfactants.

Sample	2 theta / deg.	d_{00l} / nm	D / nm
SDP-Na_xWO_3	2.34	3.77 (001)	3.77
	4.76	1.85 (002)	3.70
	7.18	1.23 (003)	3.69
CTAB-Na_xWO_3	3.68	2.40 (001)	2.40
	7.30	1.21 (002)	2.42
	10.64	0.830 (003)	2.49

The thermoelectric properties including the electrical and thermal properties were measured. The electrical conductivity σ, the Seebeck coefficient S, and the power factor PF were measured at the temperature range from 100 to 800 °C in an argon atmosphere on an Ozawa Science RZ2001i apparatus using a four-probe method and a temperature differential method. The thermal conductivity of the sintered samples was obtained using the equation $\kappa = \alpha C_p d_s$, where α is thermal diffusivity, C_p is the specific heat, and d_s is the sample density. α and C_p were measured in vacuum simultaneously utilizing the laser-flash method on a Kyoto Electronics LFA-502. The electronic thermal conductivity was calculated following the Wiedemann-Franz law $\kappa_{ele} = \sigma LT$, where L is the Lorenz number (2.44×10^{-8} V^2K^{-2}). The lattice thermal conductivity was obtained from a difference between the total and electronic thermal conductivity.

3. Results and discussion

3.1 Preparation of lamellar structure

In order to confirm the existence of the lamellar structure, PXRD was utilized as a primary technique to detect the long-range ordered structure in the samples and the results are shown in Fig. 1. The XRD patterns of both samples synthesized in the presence of the surfactant molecules clearly showed a series of sharp peaks at low angles (2 theta < 10 deg.), which were absence in the case

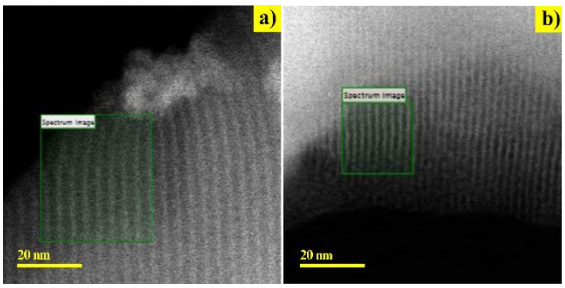

Fig. 2: STEM images of (a) SDP-Na_xWO_3 and (b) CTAB-Na_xWO_3. EDS analysis was done on the green areas on each image.

of the sample prepared via a normal reduction reaction with no surfactant. The first peak at the lowest angle represents the diffraction from the first plane, and d_{001} was calculated from the diffraction angle using Bragg's law. The interplanar distances were estimated as shown in Table. 1. Although the SDP has shorter aliphatic chain with only 12 carbons in comparison to the CTAB with 16 carbons, the calculated *d* spacing of SDP-Na_xWO_3 sample is much larger than that of the CTAB-Na_xWO_3 sample. This reflects on the different structures of the organic bilayers contained in the two samples. It should be noted that the self-assembly bilayer structure can form with interdigitated and/or with a tilted angle[27] depending on experimental conditions.

Further investigation on the layered structure of the surfactant molecules and tungsten oxide was carried out by STEM. Alternating bright and dark areas—indicating the contrast of electron density inside the compound—were observed on both samples. The bright area was assumed to be the inorganic layer with more intense electron scattering, and the dark area was assumed to be the organic one. However, the EDS results of the green area in Fig. 2(a) revealed that the bright area of the SDP-Na_xWO_3 sample contained only P and Na, which are the elements found in the hydrophilic head group and the counter ion of SDP, respectively. On the other hand, W and O were observed in the bright area of the CTAB-Na_xWO_3 sample in Fig. 2(b), and the dark area was associated with C of the CTAB molecules. Na and N at low concentrations unable to be observed on EDS were detectable with different techniques as mentioned later.

It was therefore concluded that the lamellar structure constructed with surfactant bilayer and tungsten oxide was obtained only for the CTAB-Na_xWO_3 sample. From this point onwards, the discussion will focus exclusively on this sample.

The interplanar distance of the CTAB-Na_xWO_3 sample was also calculated from the STEM image by using ImageJ software. The calculated value was 2.37 nm which is close to the *d* spacing value obtained from the XRD patterns. Nevertheless, the chain length of a single CTAB molecule is normally 1.5-2 nm. If the surfactant molecules form a non-interdigitated bilayer structure, the thickness without inorganic layer would already exceed 2.37 nm. The CTAB bilayer formed in these conditions is hence

likely to be interdigitated.

Microstructure and elemental composition of the CTAB-Na_xWO_3 sample was studied by FE-SEM-EDS. A stack of plate-like structures was observed. The size of one unbroken plate is as large as 4 μm^2. The EDS mappings of the sample also showed a homogenous distributions of Na, O, and W elements in a micrometer scale. Moreover, the atomic percentage of each detected element is shown in Table 2, and the atomic ratio of Na:W was calculated as 0.12:1. Although N was not detected by the FE-SEM-EDS due to a low concentration of N in the sample and peak overlapping with that of C, the presence of N was affirmed in XPS and FT-IR.

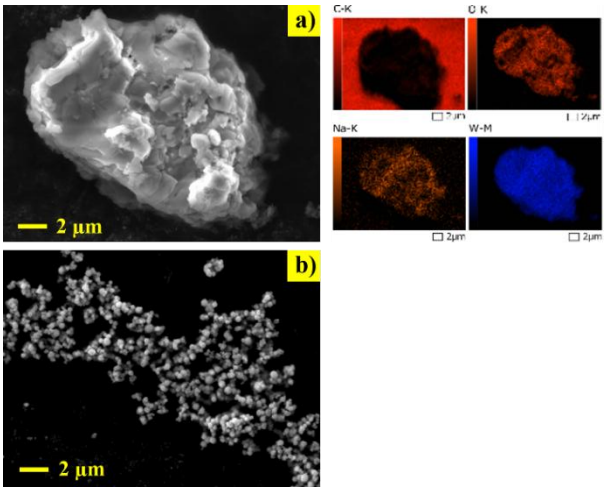

Fig. 3: FE-SEM images of (a) CTAB-Na_xWO_3 and (b) Na_xWO_3 synthesized without surfactant. EDS mappings of CTAB-Na_xWO_3 also shows distributions of 4 elements, including C, O, Na and W.

Atomic percentages of C, O, Na, W, and N were also estimated from their peak areas on the wide range XPS spectra. Na:W ratio calculated from this technique is 0.18:1 which is slightly higher than the ratio obtained from the EDS analysis. In addition, the number of surfactant molecules per one metal ion approximated from the ratio between N and W atomic percentages is around 1.

Overall, the results suggest that lamellar structure of Na_xWO_3 was successfully prepared with a long-range order via CTAB self-assembly template assisted reduction reaction.

3.2 Inorganic-organic interlayer interaction

The inorganic part of CTAB-Na_xWO_3 consisting of nonstoichiometric tungsten oxide framework was studied on XPS. The XPS spectra of W 4f (W $4f_{7/2}$ and W $4f_{5/2}$) and O 1s were obtained and fitted with constraints (Fig. 4(a)), including equal full width half maximum (FWHM) value for each W 4f and O 1s core-level spectrum, fixed peak area ratios (W $4f_{7/2}$: W $4f_{5/2}$ = 4 : 3), and fixed peak positions (ΔBE(W $4f_{5/2}$ –W $4f_{7/2}$) = 2.1 eV). Degree of asymmetry was also assumed to be zero between two

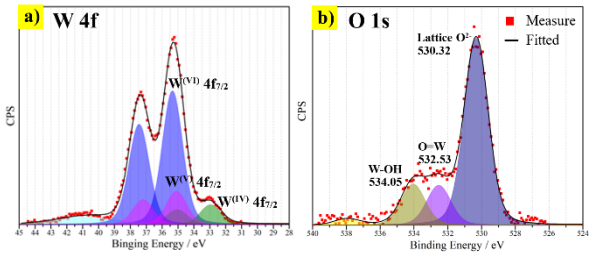

Fig. 4: XPS spectra fitting of (a) W$4f_{7/2}$ and W$4f_{5/2}$, and (b) O 1s of CTAB-Na_xWO_3 sample.

splitted W peaks. Shirley type background was utilized to analyze the W 4f spectra. As a result, the W 4f core-level spectrum was fitted with three spin−orbit doublets corresponding to the three different oxidation states of the W atoms. The fitted results confirmed a successfully reduced sample with the presence of W^V and W^{IV} species. The percentages of W^{VI}, W^V, and W^{IV} were calculated from their peak area to be 71.77%, 17.66%, and 10.56%, respectively. The peak position of W^{VI} $4f_{7/2}$ (35.35 eV) shifted from that of the pure WO_3 (36.00 eV)[28] to the lower binding energies, which is due to the weaker O-W-O bond. Meanwhile, W^V and W^{IV} appeared at the lower binding energy regions than that of the W^{VI}, as expected. In addition, the peak positions of W^V $4f_{7/2}$ (35.10 eV) and W^{IV} $4f_{7/2}$ (32.96 eV) shifted slightly to the higher binding energies, in comparison to that of the sample synthesized without surfactant molecules. This is owing to an interaction with the organic part containing an electron-attracting trimethylammonium head group (N^+Me_3). A similar situation was observed in the O 1s spectra (Fig. 4(b)) with the main peak located at 530.32 eV. The largest O 1s peak is assigned to that of the lattice O^{2-} (O-W). The slight shift from that of the sample with no surfactants to the higher binding energies is also ascribed to the intermolecular bonding between the N^+ head group of the CTAB molecule and O from the tungsten oxide. The interaction between organic and inorganic parts was further examined by FT-IR.

Table 2. Elemental analysis of the CTAB-Na_xWO_3 sample.

Elements	Mass%	Atomic%
C	60.10 ± 0.02	86.95 ± 0.03
O	9.05 ± 0.02	9.83 ± 0.02
Na	0.45 ± 0.00	0.34 ± 0.00
W	30.40 ± 0.06	2.87 ± 0.01

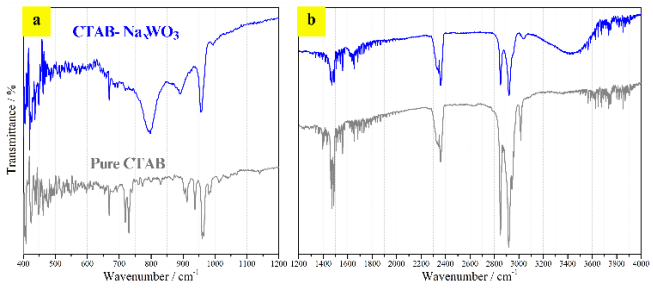

Fig. 5: FT-IR spectra of CTAB-Na_xWO_3 sample and pure CTAB at (a) low and (b) high frequency regions.

The FT-IR spectra of the CTAB-Na_xWO_3 sample showed different spectra profile from that of the pure surfactant (Fig. 5). Broad bands at low and high-frequency regions are the most distinguishable bands observed only in the lamellar sample. However, some signature bands of CTAB are still present in the layered sample.

At the low-frequency region, the appearance of $\delta_{as}(N^+Me_3)$ and $\nu(C\text{-}N^+Me_3)$ bands at 956 and 927 cm^{-1}, respectively, indicated the presence of the surfactant molecules with quaternary ammonium ions inside the sample[29]. Shifting of $\nu(C\text{-}N^+Me_3)$ band in the sample to the lower frequencies than that of the pure CTAB (937 cm^{-1}) was a consequence of the interaction between the organic head group (N^+Me_3) and the inorganic part, which weakens the bond between C and N^+Me_3 in a CTAB molecule. The information obtained from the low-frequency region was in a good agreement with the XPS results discussed in the previous paragraph. Additionally, medium to strong broad peaks at 797 and 892 cm^{-1} – corresponding to the ν(O-W-O) and ν(W=O) modes, respectively—agreed well with the XPS and FE-SEM-EDS results in the existence of the tungsten oxide structure.

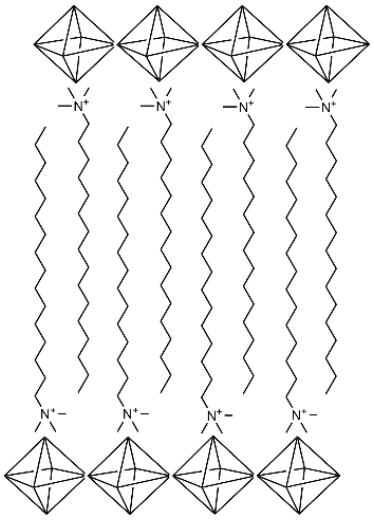

Fig. 6: A model of lamellar CTAB-Na_xWO_3 formed via self-assembly molecular template assisted reduction reaction.

In comparison to the ν(O-W-O) band of tungsten oxide (WO_3) and layered tungstic acid (H_2WO_4), the peak position of CTAB-Na_xWO_3 sample was in between these two compounds (between 824 and 740 cm^{-1})[30]. Hence, it is possible that the O-W-O bond strength and/or the alignment of the tungsten oxide layer in the sample is between that of WO_3 and H_2WO_4. Likewise, the ν(W=O) band found at a lower frequency than that of H_2WO_4 (950 cm^{-1})[30] demonstrated the weaker W=O bond in the lamellar sample than that of the H_2WO_4. This is in accordance with the XPS spectra of W 4f and O 1s indicating the intermolecular bonding between O of the W=O and the N^+Me_3 head group of CTAB. The inorganic layer could consist of more than one layer of corner-sharing [WO_6] with some intercalated H_2O molecules as the ν(O-H) broad band was also present at 3410 cm^{-1}.

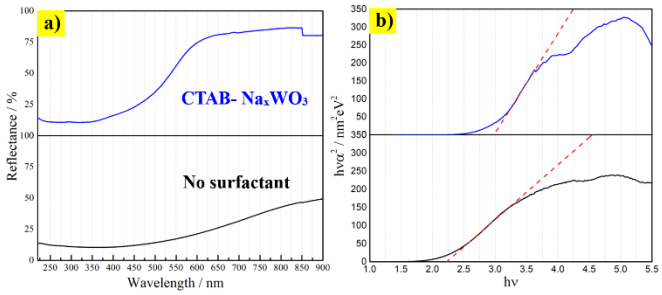

Fig. 7: (a) Diffuse-reflectance UV-Vis (DRUV) spectra and (b) the Tauc plots of CTAB-Na_xWO_3 and Na_xWO_3 without surfactant.

At the high-frequency region, the presence of the terminal quaternary ammonium ions was further confirmed by the $\nu(N^+Me_3)$ band at 3036-3039 cm^{-1}. The shift of this band to the higher frequencies suggests a stronger bond between N^+Me_3 and O than that of the Br^--N^+Me_3 in pure CTAB. Moreover, splitting of the $\delta(\text{-}CH_2\text{-})$ peak into two peaks at 1471 and 1488 cm^{-1} indicates lateral interchain interactions between contiguous CH_2 groups, specifically in the interdigitated structure[27]. Therefore, these results and the interplanar distance calculated from the XRD patterns and the STEM image support the CTAB-Na_xWO_3 model with an interdigitated bilayer structure (Fig. 6).

3.3 Optical properties

The diffuse-reflectance UV-Vis (DRUV) spectra of the lamellar Na_xWO_3 sample were obtained at the range of wavelength from 220 to 900 nm in comparison to that of the Na_xWO_3 synthesized without surfactant. As both samples are yellowish to brownish in color, their DRUV spectra show similar profiles with high reflectance percentage at longer wavelength. To determine the optical bandgap (E_g), the Tauc plots of both samples were plotted following this expression: $h\nu\alpha^{1/n} = A(h\nu\text{-}E_g)$, where h is Planck's constant, ν is the frequency of light, α is the absorption coefficient, E_g is the band gap, A is a proportional constant, and n is nature of sample transition (n=1/2 was used in this calculation). As shown in Fig. 7, E_g was calculated from the slope of a particular region on the plot marked with the red dashed line. The obtained E_g value of the lamellar Na_xWO_3 sample and the Na_xWO_3 synthesized without surfactant is 3.00 eV and 2.27 eV, respectively. The increase of E_g is due to the nano-sized organic layer between each tungsten oxide bronze layer, and hence, possibly widen the band gap of the bulk counterpart. As the optical bandgap is usually lower than the transport bandgap, we can expect the electrical bandgap to be larger than 3.00 eV for the lamellar Na_xWO_3 sample.

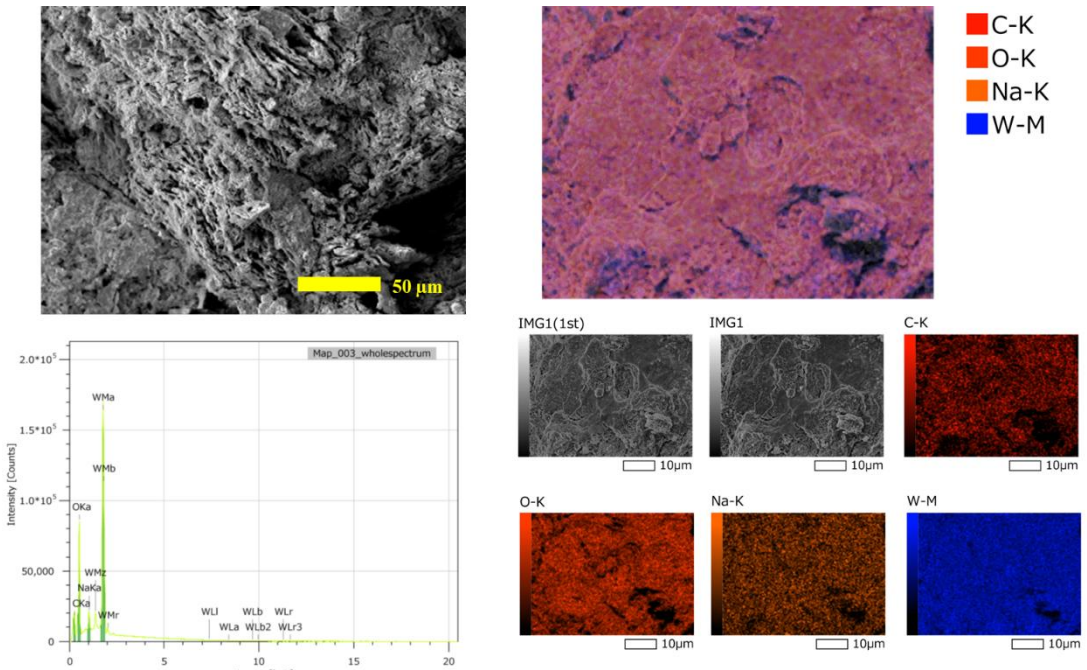

Fig. 8: An SEM image and EDS mappings of CTAB-Na_xWO_3 after being heated at 350℃ for 2 h in air.

Table 3. Elemental analysis of CTAB-Na_xWO_3 after sintering.

Elements	Mass%	Atomic%
C	9.67 ± 0.01	42.47 ± 0.04
O	9.15 ± 0.01	30.17 ± 0.04
Na	2.03 ± 0.01	4.65 ± 0.02
W	79.16 ± 0.08	22.72 ± 0.02

Table 4. Elemental analysis of CTAB-Na_xWO_3 after sintering.

Elements	Mass%	Atomic%
C	2.34 ± 0.00	14.73 ± 0.03
O	8.89 ± 0.01	42.48 ± 0.05
Na	2.31 ± 0.01	7.59 ± 0.02
W	86.46 ± 0.07	35.60 ± 0.03

3.4 Thermoelectric properties

The EDS mappings suggested that almost all of the organic part was successfully removed after heating the sample at 350℃ for 2 h (Fig. 8). Moreover, the Na to W ratio of 0.2:1 was obtained from the EDS mappings (Table 3 and 4) for the sintered sample. The XRD patterns of the sintered sample showed the presence of WO_2, Na_xWO_3, and W metal (Fig. 9). The fractions of each phase were calculated as 61.06, 34.02, and 4.92% for WO_2, Na_xWO_3, and W, respectively. Thus, the x value in the sodium tungsten bronze phase (Na_xWO_3) is 0.58. The SEM images also revealed stacks of plate-like morphology distributing randomly in the porous sintered sample (Fig. 10 and 11). Hence a bulk sample of WO_2-Na_xWO_3 mixture with partially ordered structure was prepared.

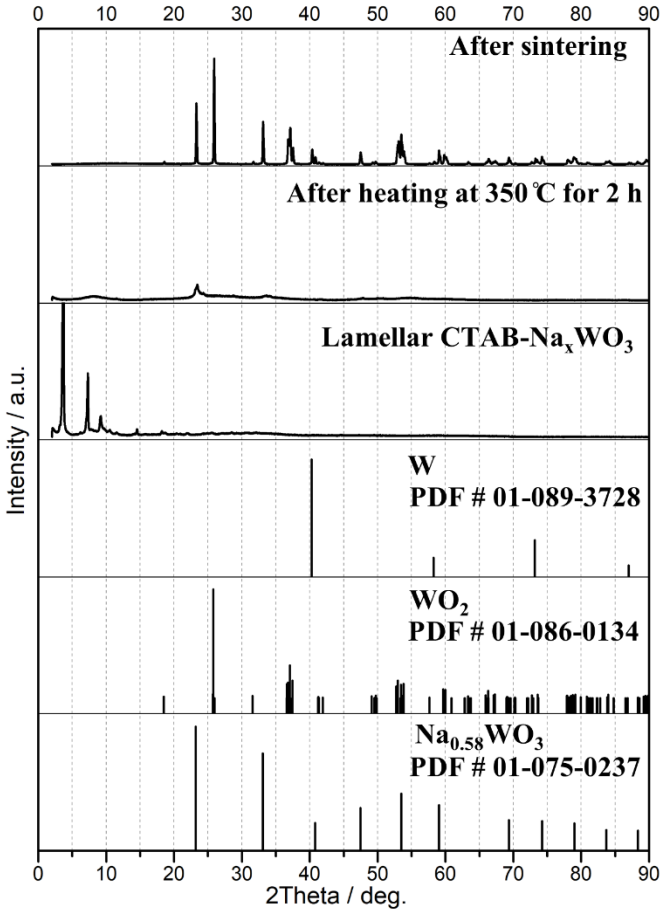

Fig. 9: XRD patterns of CTAB- Na_xWO_3, CTAB-Na_xWO_3 after being heated at 350℃ for 2 h in air, and CTAB- Na_xWO_3 after sintering.

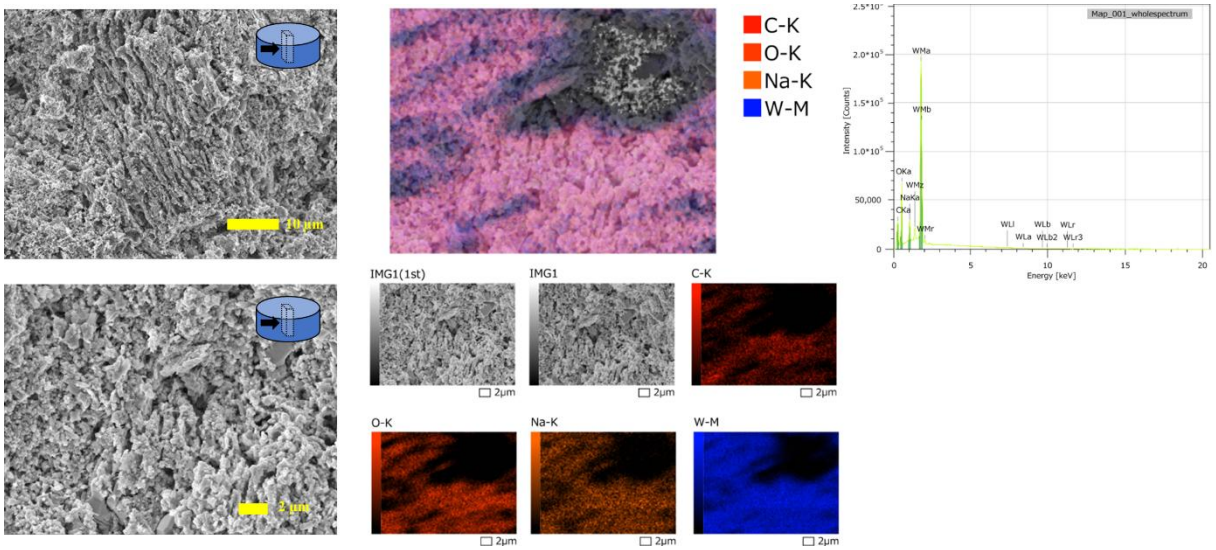

Fig. 10: SEM images and EDS mappings of CTAB-Na_xWO_3 after sintering.

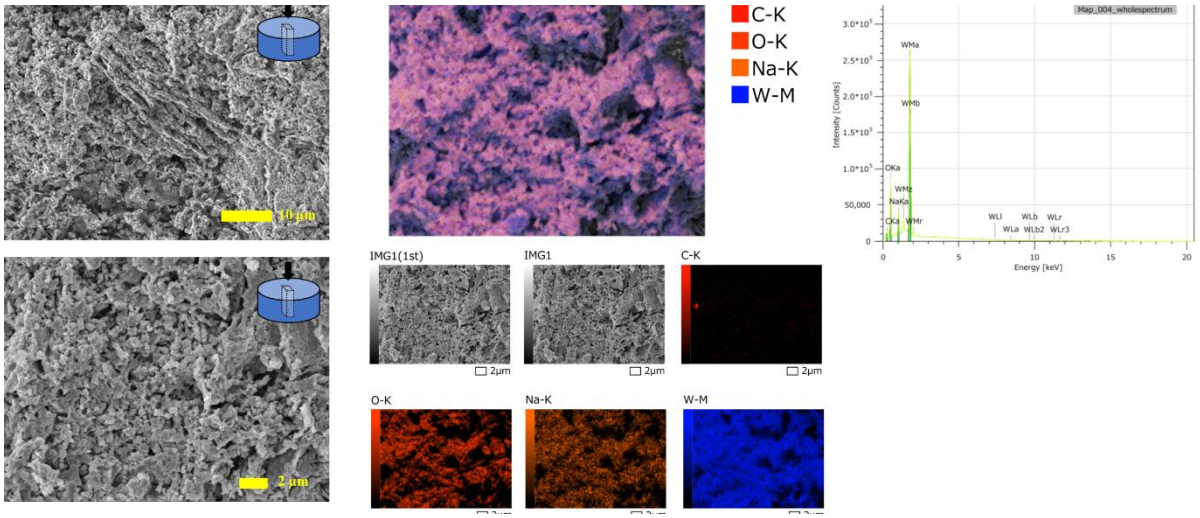

Fig. 11: SEM images and EDS mappings of CTAB-Na_xWO_3 after sintering.

The maximum electrical conductivity of ~4.1 × 10^2 S cm^{-1} was obtained (Fig. 12(a)). The range of values is considerably low in comparison to those of the reported WO_2[2)] and Na_xWO_3[5,31)] compounds. The main reason could be the low density (4.5 g cm^{-3}) and porous structure of the samples. The electrical conductivity also exhibited hysteresis, possibly due to oxygen vacancies or defects in the material that trap electrons as the temperature decreases. Consequently, lower electrical conductivities were observed during the cooling cycles of both samples before gradually approaching the values obtained during the heating cycles toward the end. However, the Seebeck coefficient of the sintered sample (Fig. 12(b)) was proven to be higher than that of the bulk WO_2 (-7 to -20 μV K^{-1})[2)] and bulk $Na_{0.47}WO_3$ (-10 to -22 μV K^{-1}) materials. This behavior contradicts to the general trend of the Seebeck coefficient in the Na_xWO_3 system, in which the compounds with higher x usually exhibit lower absolute values of the Seebeck coefficient[32)]. It is possible that the remaining ordered structure in the sintered sample played an important role in this enhancement. The power factor of the samples is shown in Fig. 12(c) with the highest value of 3.8 × 10^{-5} W K^{-2} m^{-1}. Furthermore, low thermal conductivity was also illustrated in Fig. 8(d) with the lowest values of 2.2 and 1.7 $Wm^{-1}K^{-1}$ for the total and lattice thermal conductivities, respectively. The samples exhibited thermal conductivities at least five times lower than those reported for the Na_xWO_3 (x=0.51-0.86) single crystals (> 10 W m^{-1} K^{-1})[33)] at 300K. Additionally, the samples also showed lower total thermal conductivity than that of the WO_2 (12–22 W m^{-1} K^{-1})[2)], $WO_{2.72}$ (>10 W m^{-1} K^{-1})[2)], and $WO_{2.90}$ (3.5–4.5 W m^{-1} K^{-1})[2)] within the same temperature range. The low thermal conductivity of the samples could be attributed to the samples' high porosity, retained nanostructures, and increased phonon scattering caused by small grain sizes (Fig. 10 and 11).

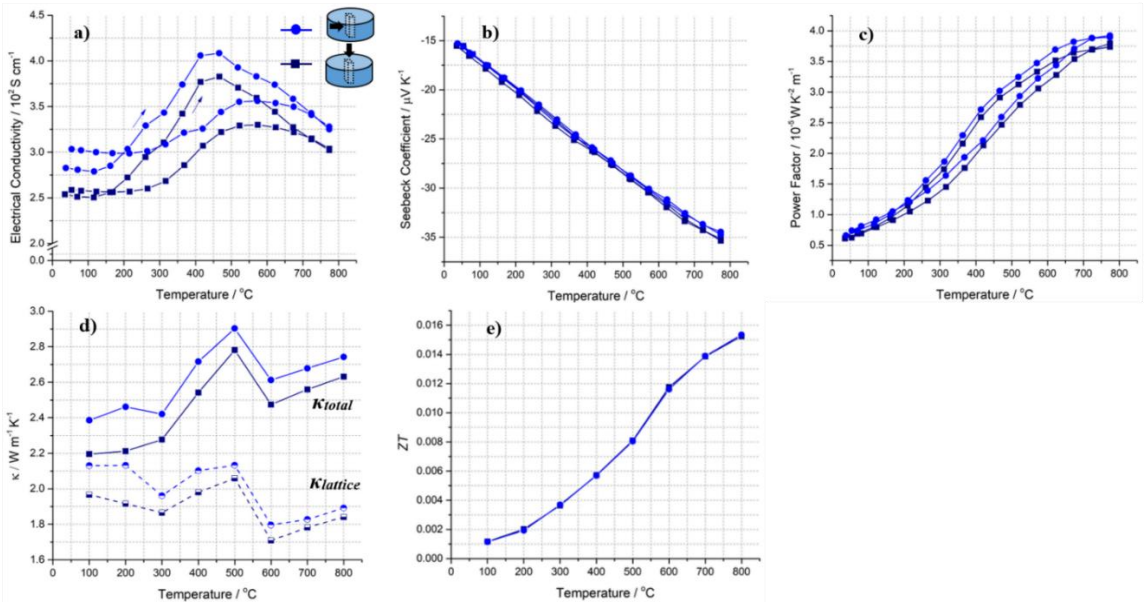

Fig. 12: Temperature dependence of the thermoelectric properties of the sintered sample measured along the directions parallel and perpendicular to the pressure; (a) the electrical conductivity, (b) the Seebeck coefficient, (c) the power factor, (d) the thermal conductivity, and (e) the *ZT* value.

The thermal and electrical conductivities of the samples, measured in two different directions, exhibited an anisotropic effect. Notably, after undergoing the conventional sintering process in the furnace, the pellet experienced shrinkage, particularly in the same direction as the measurement, as indicated by the blue circle symbols in Fig. 8. Furthermore, SEM images (Fig. 10 and 11) did not reveal any distinct grain alignment differences between the two directions. Thus, this suggests that the slightly higher thermal and electrical conductivities observed in one direction could be attributed to a higher degree of densification in that specific orientation. However, the calculated *ZT* values showed no significant difference between the two directions. Due to the low electrical conductivity and hence low power factor, in comparison to that of other well-known oxide thermoelectric materials[34-36], relatively low *ZT* values with the maximum value of 0.015 was obtained at 800℃.

4. Conclusions

The lamellar sodium tungsten bronze was successfully fabricated via a fast and simple reduction reaction of Na_2WO_4 in the presence of CTAB as a suitable surfactant for bilayer micellar template. The concentration ratio between CTAB and metal ions before the reaction was 0.3:1. As a result, interplanar distance obtained from XRD patterns (around 2.42 nm) agrees well with the value estimated from the STEM image. The organic part consists of an interdigitated CTAB bilayer with a free N^+Me_3 head group. The existence of a tungsten oxide layer was also confirmed by the presence of W and O on STEM-EDS, and the presence of ν(O-W-O) and ν(O=W) bands in the FT-IR spectra. Moreover, the XPS spectra and the FT-IR results suggest that there is an intermolecular bonding between N^+Me_3 head group of CTAB and O of the tungsten oxide layer with the atomic ratio of the surfactant molecules to the tungsten ions as 1:1. The optical bandgap energy of 3.00 eV was obtained for the lamellar sample, which is higher than that of the Na_xWO_3 synthesized via the same method but without the surfactant.

This fabrication technique provides a facile bottom-up approach to prepare a distinct lamellar structure of Na_xWO_3 in one step. This fabricating route could also allow us to achieve a tunable interplanar distance by changing the chain length of surfactant molecules. Moreover, the same method could be applied to different tungsten bronze compounds, for example, Cs_xWO_3, Rb_xWO_3, and K_xWO_3.

As proven by the improvement in the Seebeck coefficient, this type of structure possesses unconventional electrical transport properties even after the removal of the organic templating moiety. The layered structure shows high potential in improving thermoelectric properties, especially in the materials possessing high electrical conductivity, but low Seebeck coefficient. In addition, achieving higher density and higher electrical performance while maintaining partially ordered structure should be realized to further improve the overall thermoelectric properties of the samples.

Nomenclature

δ_{as}	Asymmetric bending mode
δ	Bending mode

v_{as} Asymmetric stretching mode
v Symmetric stretching mode

References

1) G. L. Frey, A. Rothschild, J. Sloan, R. Rosentsveig, R. Popovitz-Biro, and R. Tenne, "Investigations of nonstoichiometric tungsten oxide nanoparticles," *J. Solid State Chem*, 162 (*2*) 300-314 (2001). doi: 10.1006/jssc.2001.9319.
2) F. Kaiser, P. Simon, U. Burkhardt, B. Kieback, Y. Grin, and I. Veremchuk, "Spark Plasma Sintering of Tungsten Oxides WO_x ($2.50 \leq x \leq 3$): Phase analysis and thermoelectric properties," *Crystals*, 7 (*9*) 271 (2017). doi:10.3390/cryst7090271.
3) M. Zhang, C. Yang, Z. Zhang, W. Tian, B. Hui, J. Zhang, and K. Zhang, "Tungsten oxide polymorphs and their multifunctional applications," *J. Colloid Interface Sci.*, 300 102596 (2022). doi:10.1016/j.cis.2021.102596.
4) A. S. Ribnick, B. Post and E. Banks, "Phase Transitions in Sodium Tungsten Bronzes," *Adv. Chem.*, 39 246-253 (1963). doi:10.1021/ba-1964-0039.ch023.
5) P. G. Dickens and M. S. Whittingham, "The Tungsten Bronzes and Related Compounds," *Q. Rev. Chem. Soc.*, 22 30-44 (1968). doi:10.1039/QR9682200030.
6) H. R. Shanks, P. H. Sidles and G. C. Danielson, "Electrical Properties of the Tungsten Bronzes," *Adv. Chem.*, 39, 237-245 (1963). doi:10.1021/ba-1964-0039.ch022.
7) S. Raj, T. Sato, S. Souma, T. Takahashi, D. D. Sarma and P. Mahadevan, "Metal-insulator transition of Na_xWO_3 studied by angle-resolved photoemission spectroscopy," *Mod. Phys. Lett. B*, 23 (*24*) 2819-2846 (2009). doi:10.1142/s0217984909021004.
8) M. E. Straumanis, "The sodium tungsten bronzes. I. chemical properties and structure," *J. Am. Chem. Soc.*, 71 (*2*) 679–683 (1949). doi:10.1021/ja01170a085.
9) L. D. Muhlestein and G. C. Danielson, "Effects of Ordering on the Transport Properties of Sodium Tungsten Bronze," *Phys. Rev.*, 158 825-832 (1967). doi:10.1103/PhysRev.158.825.
10) L. Chao, C. Sun, J. Dou, J. Li, J. Liu, Y. Ma, and L. Xiao, "Tunable transparency and NIR-shielding properties of nanocrystalline sodium tungsten bronzes," *Nanomaterials*, 11 (3) 731 (2021). doi: 10.3390/nano11030731.
11) T. Gao, and B. P. Jelle, "Electrochromism of hexagonal sodium tungsten bronze nanorods," *Sol. Energy Mater. Sol. Cells.*, 177 3-8 (2018). doi:10.1016/j.solmat.2017.11.025.
12) L. Tegg, D. Cuskelly, and V. J. Keast, "The sodium tungsten bronzes as plasmonic materials: fabrication, calculation and characterization," *Mater. Res. Express*, 4 065703 (2017). doi:10.1088/2053-1591/aa6c40.
13) L. Wang, J. Zhan, W. Fan, G. Cui, H. Sun, L. Zhuo, X. Zhao, and B. Tang, "Microcrystalline sodium tungsten bronze nanowire bundles as efficient visible light-responsive photocatalysts," *Chem. Commun.*, 46 8833-8835 (2010). doi:10.1039/C0CC03660A.
14) B. W. Brown, and E. Banks, "The sodium tungsten bronzes," *J. Am. Chem. Soc.*, 76 (*4*) 963-966 (1954). doi:10.1021/ja01633a004.
15) X. Li, R. Xie, X. Cao, L. Liu, L. Xu, Y. Wang, C. Meng, and Q. Wu, "Synthesis of cubic sodium tungsten bronze Na_xWO_3 in air," *J. Am. Ceram. Soc.*, 101 (*10*) 4458-4462 (2018). doi: 10.1111/jace.15740.
16) C. T. Hauck, A. Wold, E. Banks, R. Seiver, and H. A. Eick, "Sodium tungsten bronzes," *Inorganic Syntheses* 12 153-158 (1970). doi: 10.1002/9780470132432.ch27.
17) J. Hou, G. Zuo, G. Shen, H. Guo, H. Liu, P. Cheng, J. Zhang, and S. Guo, "Hollow sodium tungsten bronze ($Na_{0.15}WO_3$) nanospheres: preparation, characterization, and their adsorption properties," *Nanoscale Res Lett.*, 4 (*10*) 1241-1246 (2009). doi: 10.1007/s11671-009-9383-x.
18) J. Y. Luo, J. X. Liu, F. Shi, Q. Xu, Y. Y. Jiang, G. S. Liu, and Z. Q. Hu, "Synthesis of sodium tungsten bronze via hydrothermal method assisted by citric acid," *Adv. Mat. Res.*, 712-715 280-283 (2013), doi:10.4028/www.scientific.net/amr.712-715.280.
19) T. Martina, T. R. Machado, M. M. Ferrer, S. M. Zanetti, and E. Longo, "Facile microwave-assisted hydrothermal synthesis of hexagonal sodium tungsten bronze and its high response to NO_2," *Mater. Lett.*, 185 197-200 (2016). doi:10.1016/j.matlet.2016.08.126.
20) C. Guo, S. Yin, and T. Sato, "Synthesis of one-dimensional hexagonal sodium tungsten oxide and its near-infrared shielding property," *Nanosci. Nanotechnol. Lett.*, 3 (*3*) 413-416 (2011). doi:10.1166/nnl.2011.1182.
21) H. R. Shanks, "Growth of tungsten bronze crystals by fused salt electrolysis," *J. Cryst. Growth.*, 13-14 433-437 (1972). doi:10.1016/0022-0248(72)90199-6.
22) S. Yeu, and Y. Zhang, "Electronic transport properties of sodium tungsten bronzes $Na_{0.54}WO_3$ single crystals," *J. Mater. Sci. Technol.*, 28 (*6*) 569-571 (2012). doi:10.1016/S1005-0302(12)60099-1.
23) W. Zhang, B. Li, Y. G. Sun, A. M. Cao, and L. J. Wan, "Spherical mesoporous metal oxides with tunable orientation enabled by growth kinetics control," *J. Am. Chem. Soc.*, 142 (*42*) 17897-17902 (2020). doi:10.1021/jacs.0c07938.
24) Z. Sun, T. Liao, Y. Dou, S. M. Hwang, M. S. Park, L. Jiang, J. H. Kim, and S. X. Dou, "Generalized self-assembly of scalable two-dimensional transition metal oxide nanosheets," *Nat. Commun.*, 5 (*1*) 1-9 (2014). doi:10.1038/ncomms4813.
25) T. He, D. CHen, X. Jiao, and Y. Wang, "Co_3O_4

Nanoboxes: surfactant-templated fabrication and microstructure characterization," *Adv. Mater.*, 18 (*8*) 1078-1082 (2006). doi:10.1002/adma.200501864.

26) H. Fujii, M. Ohtaki, and K. Eguchi, "Synthesis and photocatalytic activity of lamellar titanium oxide formed by surfactant bilayer templating," *J. Am. Chem. Soc.*, 120 (*27*) 6832-6833 (1998). doi:10.1021/ja980430d.
27) S. H. Park, and C. E. Lee, "Characterization of chain molecular assemblies in long-chain, lamellar copper alkylsulfonates: self-assembled monolayer vs bilayer structure," *Chem. Mater.*, 18 (*4*) 981-987 (2006). doi:10.1021/cm052410y.
28) V.I. Nefedov, M.N. Firsov, and I.S. Shaplygin, "Electronic structures of $MRhO_2$, MRh_2O_4, $RhMO_4$ and Rh_2MO_6 on the basis of X-ray spectroscopy and ESCA data," *J. Electron Spectrosc. Relat. Phenom.*, 26 (*1*) 65-78 (1982). doi:10.1016/0368-2048(82)87006-0.
29) J. D. Anastassopoulou, "Mass and FT-IR spectra of quaternary ammonium surfactants," in *Chemistry and properties of biomolecular systems*, ed. E. Rizzarelli, and T. Theophanides (Dordrecht; Springer, 1991), 8 (*1*). doi:10.1007/978-94-011-3620-4_1.
30) B. Ingham, S. V. Chong, and J. L. Tallon, "Layered tungsten oxide-based organic−inorganic hybrid materials: an infrared and raman study," *J. Phys. Chem. B*, 109 (*11*) 4936-4940 (2005). doi:10.1021/jp045066l.
31) A. M. El-Sayed, and S. M. A. Mousa, "Some properties of sodium tungsten bronzes as a function of sodium concentration," *Indian J. Chem. Techn.,* 12 304-308 (2005).
32) L. D. Muhlestein and G. C. Danielson, "Seebeck Effect in Sodium Tungsten Bronze," *Phys. Rev.*, 160 (3) 562-567 (1967). doi:10.1103/physrev.160.562.
33) A. E. Whiteman and J. J. Martin, "Thermal Conductivity of Cubic Sodium Tungsten Bronze," *J. Phys. Chem. Solids*, 32 (9) 2223-2229 (1971). doi: 10.1016/S0022-3697(71)80401-8.
34) H. C. Wang, C. L. Wang, W. B. Su, J. Liu, Y. Sun, H. Peng and L. M. Mei, "Doping Effect of La and Dy on the Thermoelectric Properties of $SrTiO_3$," *J. Am. Ceram. Soc.*, 94 (3) 838-842 (2011). doi: 10.1111/j.1551-2916.2010.04185.x.
35) K. Park, H. K. Hwang, J. W. Seo and W.-S. Seo, "Enhanced high-temperature thermoelectric properties of Ce- and Dy-doped ZnO for power generation," *Energy*, 54 (c) 139-145 (2013). doi: 10.1016/j.energy.2013.03.023.
36) T. Tsubota, M. Ohtaki, K. Eguchi and H. Arai, "Thermoelectric properties of Al-doped ZnO as a promising oxide material for high-temperature thermoelectric conversion," *J. Mater. Chem.*, 7 85-90 (1997). doi:10.1039/A602506D.